AMSR-E Algorithm for Snowmelt Onset Detection in Subarctic Heterogeneous Terrain

J.D. APGAR[1], J.M. RAMAGE[1], R.A. MCKENNEY[2], AND P. MALTAIS[3]

ABSTRACT

Snowmelt onset in the upper Yukon River basin, Canada, can be derived from brightness temperatures (T_b) obtained by the Advanced Microwave Scanning Radiometer for EOS (AMSR-E) on NASA's Aqua satellite. This sensor, with a resolution of 14 x 8 km^2 for the 36.5 GHz frequency and two to four observations per day, improves upon the twice-daily coverage and 37 x 28 km^2 spatial resolution of the Special Sensor Microwave Imager (SSM/I). The onset of melt within a snowpack causes an increase in the average daily 36.5 GHz vertically polarized T_b as well as a shift to high diurnal amplitude variations (DAV) as the snow melts during the day and refreezes at night. The higher temporal and spatial resolution makes AMSR-E more sensitive to sub-daily T_b oscillations, resulting in DAV that often show a greater daily range compared to SSM/I. Therefore, thresholds of $T_b > 246$ K and DAV > ±10 K developed for use with SSM/I have been adjusted for detecting melt onset with AMSR-E using ground-based surface temperature and snowpack wetness relationships. Using newly developed thresholds of $T_b > 252$ K and DAV > ±18 K, AMSR-E determined snowmelt onset correlates well with SSM/I observations in the small subarctic Wheaton River basin through the 2004 and 2005 winter/spring transition. In addition, snowmelt onset derived from AMSR-E data gridded at a higher resolution than the SSM/I data indicates that finer-scale differences in elevation and land cover affect snowmelt onset and are detectable with the AMSR-E sensor. Based on these observations, the enhanced resolution of AMSR-E is more effective than SSM/I at delineating spatial and temporal snowmelt dynamics in the heterogeneous terrain of the upper Yukon River basin.

Keywords: snowmelt, passive microwave, SSM/I, AMSR-E, Yukon River, Wheaton River

INTRODUCTION

This Hydrologic and atmospheric processes are closely tied with snow characteristics throughout the arctic and subarctic regions of the Northern Hemisphere. The extent of snow cover, snow water equivalent (SWE), and the timing of spring snowmelt influence local hydrology as well as regional and global water budgets, and the high albedo of snow has an important influence on the global energy budget (Vorosmarty *et al.*, 2001). The spring snowmelt is an annual event in snow-covered, high-latitude drainage basins that sends significant quantities of meltwater downstream during a relatively short period of time. The timing and magnitude of these events are variable, but they can create a large impact on the basin hydrology and influence geomorphic change within the basin. The use of passive microwave data to examine the

[1] Earth and Environmental Sciences, Lehigh University, Bethlehem, PA 18015, USA
[2] Geosciences/Environmental Studies, Pacific Lutheran University, Tacoma, WA 98447, USA
[3] Water Survey of Canada, Environment Canada, 91782 Alaska Highway, Whitehorse, Yukon Territory, Canada Y1A 5B7

characteristics associated with this seasonal snowmelt may provide a better understanding of the sensitivity of snowmelt timing to climatic conditions as well as the effects of the snowmelt upon basin hydrology.

The Yukon River extends from the Juneau Icefield, British Columbia, to the Bering Sea, passing through the Yukon Territory and Alaska. It receives drainage from a basin more than 850,000 km^2 in area. The majority of this drainage flows from the Bering Sea northward to provide 8% of the total fluvial freshwater input to the Arctic Ocean (Aagaard and Carmack, 1989). The basin includes a variety of ecosystems as well as a range of elevations and local relief. This region has a heterogeneous terrain marked by boreal forests, mountain ranges, low-lying valleys, and a variety of lakes. Much of the upper basin is seasonally snow covered aside from some glaciated regions near the headwaters.

This paper will focus on the timing of the spring snowmelt transition in the Wheaton River sub-basin of the Yukon River (Fig. 1), from which the findings may then be applied to larger sub-basins and eventually the upper Yukon River basin as a whole. The Wheaton River basin is a small (875 km^2) upland basin that has heterogeneous topography and terrain with only a small glacial input.

Two passive microwave sensors, the Special Sensor Microwave Imager (SSM/I) and Advanced Microwave Scanning Radiometer for EOS (AMSR-E), provide at least twice daily observations in the high latitude regions, and the record of SSM/I observations extends back nearly two decades. Due to differences in brightness temperature emitted from dry versus wet snow, these passive microwave sensors are effective at differentiating between snow that is melting and snow that is not melting, or frozen. In addition, the ability of these sensors to observe snow characteristics through clouds and most other atmospheric conditions, as well as during the night, proves useful for examining snowmelt in high latitude areas that may have increased cloud cover and darkness during the winter and spring months.

The purpose of this study is to derive the timing of spring snowmelt in the Wheaton River basin with recently acquired AMSR-E observations and to test the sensitivity of this sensor to the dynamic and varied regional snowpack characteristics. A snowmelt onset algorithm developed by Ramage *et al.* (2006) for use with SSM/I data is modified for use with AMSR-E data to allow for a direct comparison of snowmelt onset timing from both of these passive microwave sensors. In addition, higher-resolution AMSR-E data and elevation data are used to show improvements of this sensor over the SSM/I sensor in detecting snowmelt within heterogeneous terrain. The algorithm is fine-tuned using hourly near-surface air temperature data and ground-based snow wetness data from within the Wheaton River basin. Due to the greater spatial and temporal resolution of the AMSR-E sensor compared to SSM/I, snowmelt dynamics can be more accurately described with AMSR-E data in the mixed terrain of the upper Yukon River basin.

DATA

Passive microwave satellites provide a means by which to differentiate between snow that is melting and snow that is frozen. Both AMSR-E and SSM/I brightness temperature data were used for this analysis. In addition, 90 meter digital elevation models of the Yukon Territory were utilized (Environment Yukon, 2000), as well as hourly temperature measurements and snow wetness measurements from within the Wheaton River basin.

AMSR-E swath data, in the form of Level-2A Global Swath Spatially-Resampled Brightness Temperatures (T_b) V001, are supplied by the National Snow and Ice Data Center (NSIDC) through the EOS Data Gateway with a record of observation that extends back to 2002 (Ashcroft and Wentz, 2004). The AMSR-E sensor provides two to four observations of the study area per

day and has a mean pixel resolution at 36.5 GHz of 12 x 12 km^2 (actual footprint size is 14 x 8 km^2). Twice-daily SSM/I data extending back to 1987 come from the Defense Meteorological Satellite Program (DMSP) SSM/I and have a nominal resolution for the 37 GHz channel of 37 x 28 km^2. SSM/I images gridded to the Equal Area Scalable Earth Grid (EASE-Grid) 25 x 25 km^2 resolution are provided by the NSIDC, and this product separates the ascending and descending passes. The AMSR-E data were gridded first at the EASE-Grid 25 x 25 km^2 resolution to compare directly with the SSM/I data and establish to what degree they are similar with a minimum of complicating factors. The AMSR-E data then were gridded at the finer EASE-Grid 12.5 x 12.5 km^2 resolution to examine improvements in snowmelt detection of AMSR-E upon the SSM/I sensor.

Passive microwave sensors have been used to examine characteristics of snow such as snow extent (e.g. Abdalati and Steffen, 1997; Walker and Goodison, 1993; Wang *et al.*, 2005), snow depth (e.g. Josberger and Mognard, 2002; Kelly *et al.*, 2003), and snow water equivalent (e.g. Derksen *et al.*, 2005; Foster *et al.*, 2005; Goita *et al.*, 2003). The SSM/I sensor has been used in previous studies to establish the timing of the spring melt transition in the upper Yukon River basin (Ramage *et al.*, 2006) as well as in the Juneau Icefield (Ramage and Isacks, 2002, 2003). Even though the SSM/I sensor provides twice-daily observations and has been shown to correlate well with ground-based brightness temperature measurements over fairly homogeneous terrain such as the Alaskan North Slope (Kim and England, 2003), the pixel resolution of greater than 25 x 25 km^2 that results from the passive nature of the sensor is a problematic issue in monitoring dynamic changes over heterogeneous terrain. The AMSR-E sensor, recently launched aboard NASA's Aqua satellite in 2002, provides more observations of the study area per day and, with an improved pixel resolution over SSM/I, can help to provide a more accurate examination of snow characteristics over mixed terrain.

A significant difference in brightness temperature (T_b) between dry and wet snow occurs at frequencies greater than 10 GHz. The T_b of a material is related to its surface temperature (T_s) and emissivity (E),

$$T_b = ET_s. \quad (1)$$

A rapid increase in emissivity occurs as a result of a small amount (~ 1-2%) of liquid water within the snowpack, causing the T_b to increase for wet snow (Ulaby *et al.*, 1986). The T_b in the 19 and 37 GHz frequencies associated with the SSM/I sensor are useful in detecting melt on glaciers (Ramage and Isacks, 2002, 2003) and on heterogeneous terrain (Ramage *et al.*, 2006) since the T_b transition from dry to wet snow occurs as surface temperatures approach 0°C. From the AMSR-E sensor, the T_b from the vertically polarized 36.5 GHz frequency (wavelength of 0.82 cm) is comparable to the SSM/I sensor for the detection of snowmelt. Here, we focus on comparing and contrasting the T_b from the two sensors and comparing the ability to detect the onset of snowmelt.

During the spring snowmelt, the snowpack experiences cyclical daytime melt and nighttime freeze, changes that are manifested as diurnal differences in T_b. As a result of the at least twice-daily observations by the sensors, these high diurnal amplitude variations of T_b (referred to as DAV) can be detected and are useful in identification of these dynamic transition periods.

The Wheaton River basin is covered by six EASE-Grid 25 x 25 km^2 pixels (Fig. 1a and Table 1). Due to the coarse pixel size in relation to the size of the basin, some pixels only cover a small percentage of the basin (see Table 1). The Wheaton basin has a range of elevations and land cover that include bare mountain slopes, dense boreal forest, and slopes of varying aspect (Brabets *et al.*, 2000; Ramage *et al.*, 2006). Pixels A02 and A03 cover the upland headwaters of the Wheaton River and have high mean elevations. The rest of the basin is mostly covered by pixels B03 and B02, representing the middle and lower parts of the basin respectively. Pixels C02 and C03 cover a small fraction of the basin but can be used to examine the lowest elevations of the basin. In

relation to the AMSR-E data gridded to the EASE-Grid 12.5 x 12.5 km^2 resolution, the Wheaton River basin is covered by parts of 14 pixels, improving the spatial scale at which differences in snowmelt characteristics can be investigated (Fig. 1b). Adjacent pixels in this area appear to have similar T_b signatures that differ only slightly due to differences in land cover as well as elevation and topography. Seasonal variations related to frost, vegetation, and lakes are also factors in this complex landscape, but snowmelt has the largest influence on T_b.

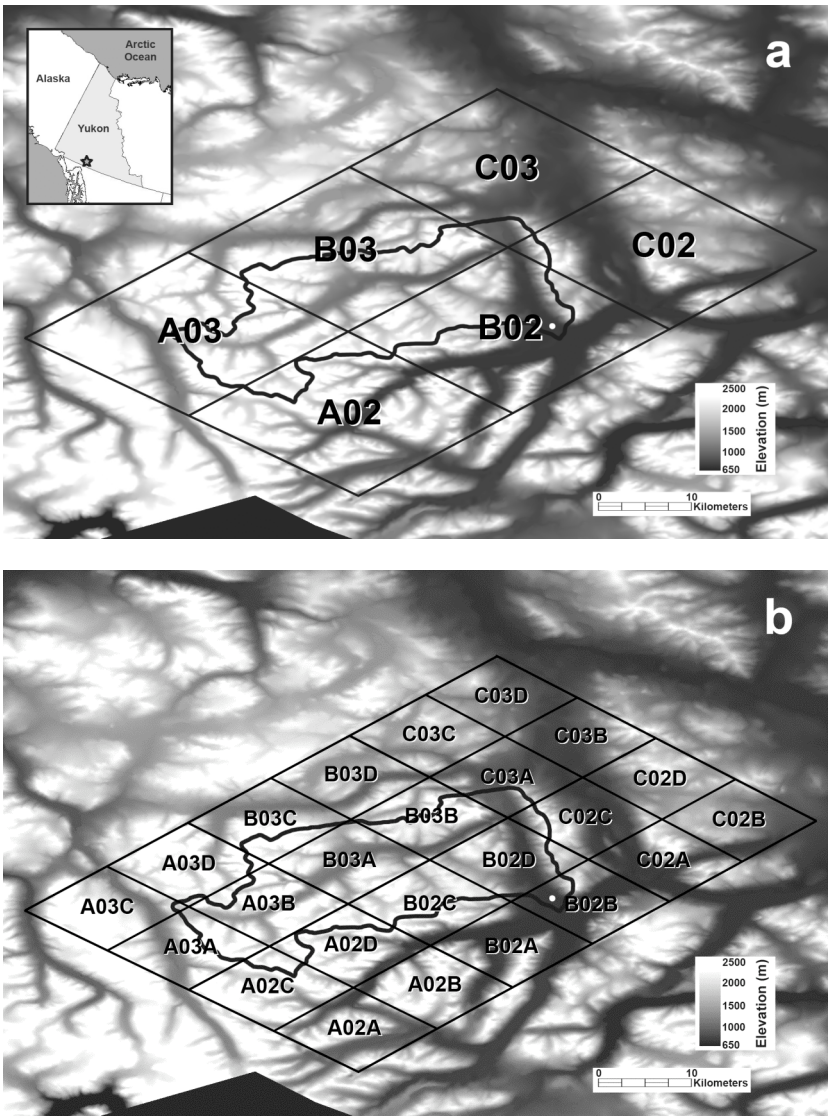

Figure 1. Wheaton River basin EASE-Grid (a) 25 x 25 km^2 pixels and (b) 12.5 x 12.5 km^2 pixels superimposed on a 1:250,000 (90 m) digital elevation model (Environment Yukon, 2000). While the actual sensor footprints are more elliptical in shape, these square pixels provide a good representation for the land area covered. The inset map shows the location of the basin within the Yukon Territory. The basin (black outline) is represented by parts of six 25 x 25 km^2 pixels and fourteen 12.5 x 12.5 km^2 pixels. The Wheaton River near Carcross stream gauge is located near the river's mouth at an elevation of 668 m (white dot in pixels B02 and B02B).

Table 1. Wheaton River basin EASE-Grid 25 x 25 km^2 pixel characteristics (from Ramage et al., 2006)

Pixel ID	EASE *X*	EASE *Y*	Latitude (°)	Longitude (°)	Mean Elevation (m)	Minimum Elevation (m)	Maximum Elevation (m)	Relief (m)	% in Wheaton Basin
A02	267	266	59.84	-135.30	1435	720	2192	1472	8
A03	268	266	60.00	-135.61	1576	802	2479	1677	30
B02	267	267	60.00	-135.30	1177	672	2193	1521	42
B03	268	267	60.17	-135.30	1373	798	2193	1395	48
C02	267	268	60.17	-134.69	1084	691	1998	1307	4
C03	268	268	60.33	-135.00	1051	717	1883	1166	6

Near-surface air temperatures for the Wheaton River basin were acquired in 2004 and 2005 using a HOBO automatic temperature logger located within pixel B02 at 668 m, approximately 10 m from Environment Canada's "Wheaton River near Carcross" stream gauge (60°08′05″N, 134°53′45″W). The HOBO recorded hourly air temperature and relative humidity and was situated about 1.5 m above the forest floor on the north facing side of a spruce tree (shaded most of the time). It was installed under a protective platform in August 2004, and data were downloaded periodically by Pat Maltais of the Water Survey of Canada.

A field campaign was carried out during the spring of 2005 to collect a variety of in situ snowpack measurements from snowpits, including snow density and the dielectric properties of the snow at various depths, at times that coincided with AMSR-E satellite overpasses. The dielectric properties of the snow, and ultimately the snow liquid water content as a percentage of the volume, were derived from these measurements to relate to AMSR-E brightness temperature data. Other observations of the snowpack in the upper Yukon River basin provided support to show that the response in T_b could be attributed to snowmelt instead of liquid precipitation events.

METHODS

Ramage *et al*. (2006) developed a snowmelt onset algorithm for use with SSM/I 37V GHz data to detect the timing of snowmelt onset within the Wheaton River basin. This algorithm determines the onset of snowmelt based on the day of the year when certain thresholds for both brightness temperature (T_b) and diurnal amplitude variation (DAV) are met (Table 2). For the SSM/I data, 'DAV Melt' occurs when DAV is greater than ±10 K, and 'Melt Onset' occurs on the day when T_b is greater than 246 K and DAV is greater than ±10 K, indicating the snow is both melting periodically and experiencing strong melt-refreeze cycles (Ramage and Isacks, 2002, 2003). In addition, 'End DAV' represents the end of the transition when DAV decreases below ±10 K, and the duration of the transition period is calculated as the number of days between 'Melt Onset' and 'End DAV'.

Table 2. Snowmelt onset thresholds

Sensor	Tb (K)	DAV (±K)
SSM/I	246	10
AMSR-E	252	18

A number of assumptions must be made in detecting snowmelt onset using this passive microwave data. The heterogeneous and mountainous terrain within the upper Yukon River basin most likely creates a complex T_b signal, but based largely on field observations and local weather records, it is assumed that the majority of the land is covered with snow during the spring transition period. In addition, since the methods focus on snowmelt events during the spring transition from March through May, intermittent snowmelt and thaw events during the winter months are largely ignored. It is also assumed, based on support from field data, that the events identified with the passive microwave data as melting snow are representative of snowmelt and not liquid precipitation events.

AMSR-E swath data were processed using the AMSR-E Swath-to-Grid Toolkit (AS2GT) in NSIDC's Passive Microwave Swath Data Tools (PMSDT). The data were then gridded to the EASE-Grid Northern Hemisphere projection with a nominal resolution of 25 x 25 km^2, the same format and pixel resolution as the SSM/I data provided by the NSIDC. The T_b were extracted from each channel using Interactive Data Language (IDL) code, creating a chronological time series of all T_b observations for 2004 and 2005.

Since there are two to four AMSR-E observations per day, DAV cannot simply be calculated as the difference from one observation to the next, as is done with the twice-daily SSM/I observations. Extra observations in a given day are often less than 2.5 hours from the previous one and have fairly similar T_b (Fig. 2). These extra values cause the DAV to artificially approach 0 K as a result of similar T_b values even if the actual daily oscillation is much greater. An alternative to the raw data is to average the observations that are less than 2.5 hours apart (Fig. 2). This creates a total of two observations for each day and eliminates extraneous DAV values that approach 0 K, allowing for more representative DAV values to be calculated and used for examining snowmelt characteristics in a similar way to SSM/I DAV. Other techniques used to calculate DAV, including using daily minimum and maximum values, did not provide representative diurnal variations as well as the above method. The absolute value of DAV is used since DAV can be either positive or negative. For the purposes of examining snowmelt, only the 36.5 GHz vertically polarized observations were used.

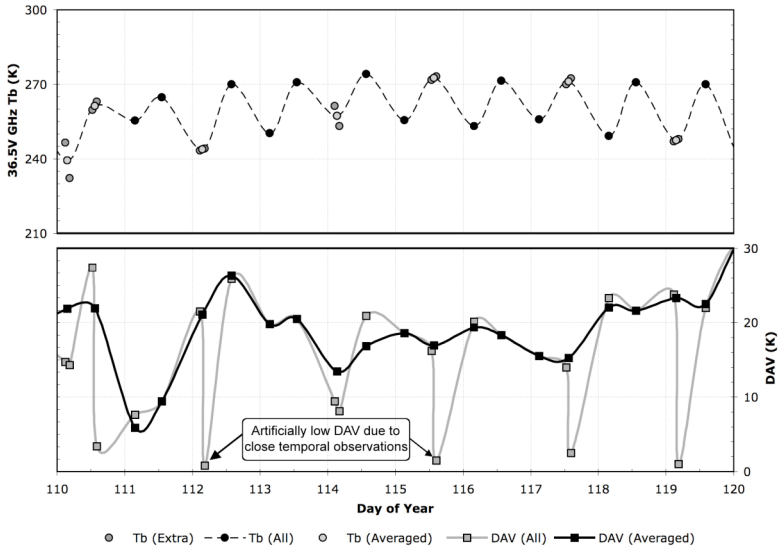

Figure 2. Calculation of DAV from AMSR-E 36.5V GHz T_b. In order to examine daily fluctuations, T_b less than 2.5 hours apart (medium gray circles) were averaged. The running differences of these observations with the other observations produces a more accurate DAV representation (solid black line) than if all observations are used to calculate daily variations (gray line).

The SSM/I snowmelt onset algorithm was modified for use with AMSR-E 36.5 GHz vertically polarized T_b data. Initial examination of this data from the AMSR-E sensor for 2005 indicated that the observations were more sensitive to daily fluctuations and that the previous T_b snowmelt threshold for SSM/I of 246 K was too low. To develop a new threshold for the snowmelt onset algorithm, the AMSR-E 36.5V GHz T_b for the six Wheaton River basin pixels were plotted against temporally-corresponding near-surface air temperature data from the Wheaton River for the period of August 2004 to December 2005 (Fig. 3). When the air temperature is near 0°C, the T_b rapidly increases due to the presence of liquid water in the snowpack. The T_b at which this transition from frozen to melting snow occurs is considered the threshold. A histogram of annual AMSR-E 36.5V GHz T_b data was also produced to identify the new T_b threshold (Fig. 4). A typical year of observations in this seasonally-snow covered region has a bimodal distribution of T_b related to frozen, dry snow during the cold months and wet snow or no snow during the warmer months, and the T_b that separates these two conditions is the T_b threshold (Fig. 4, Table 2).

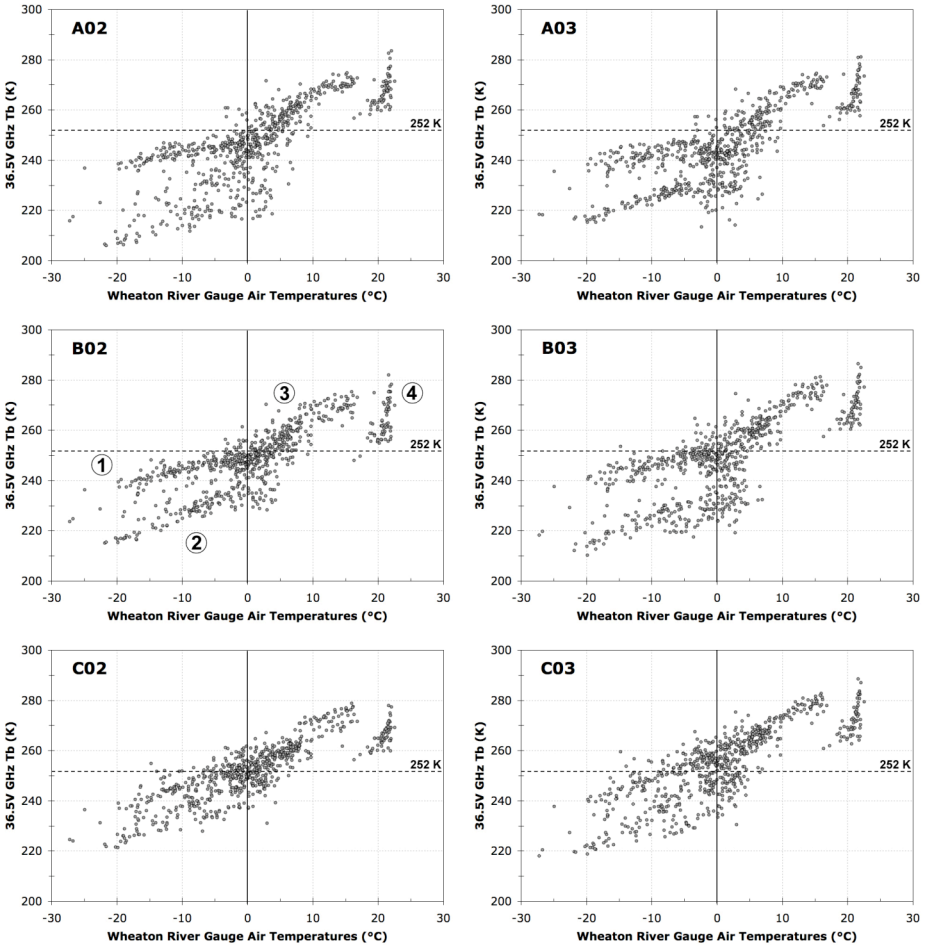

Figure 3. Scatterplots of Wheaton River near-surface air temperatures compared to AMSR-E 36.5 GHz vertically polarized T_b for the six 25 x 25 km^2 Wheaton River basin pixels for 2004-2005. The transition in T_b from frozen (1,2) to melting (3) snow, which appears as an inflection in the slope near a surface temperature of 0°C, helps to establish the T_b threshold of snowmelt as 252 K. The two unique distributions that exist at temperatures below 0°C in most of the pixels (1,2) may be related to snowpack grain size growth or the presence of ice on vegetation. The area of high temperatures (4) represents snow-free surfaces during the summer months.

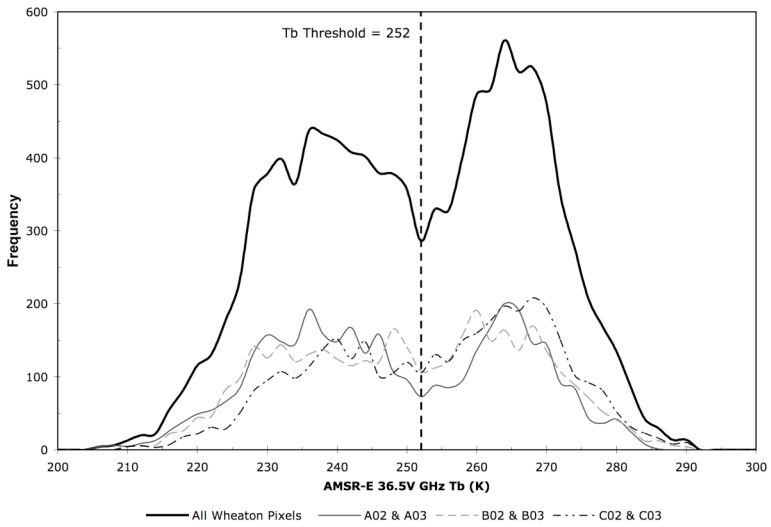

Figure 4. Frequency histogram of all AMSR-E 36.5V GHz T_b for the six Wheaton River basin 25 x 25 km^2 pixels during the 2004-2005 period. The T_b are grouped in bins of 2 K. The bimodal distribution suggests a threshold of 252 K is more suitable for distinguishing between frozen (left distribution) and wet (right distribution) snow using AMSR-E in the Wheaton River basin than the SSM/I threshold of 246 K. The individual pixel sets, while not as clearly defined, also have minima near the threshold of 252 K.

Measurements of snowpack properties were obtained in the Wheaton River basin during the spring of 2005. More than fifty snowpits were dug in a variety of locations, encompassing a range of elevations, terrains, and forest cover in an attempt to represent the heterogeneous nature of the region. Characteristics of the snowpack were described and measured, including the general stratigraphy as well as grain size, air and snow temperature, and snow structure at various depths. A comprehensive analysis of these parameters is beyond the scope of this paper. A snow surface dielectric capacitance probe and measurements of snow density were used to derive snow wetness as a percentage of the volume at different depths (Denoth, 1989). Surface and near-surface wetness values were averaged from multiple measurements at each site, and these wetness values were later compared with AMSR-E 36.5V GHz T_b from overpasses obtained less than one hour before or after the ground observations (Figs. 5a and 5b, Table 3). In addition to supporting the new T_b threshold, these observations helped show that the observed T_b response is linked to melting snow and is not the result of liquid precipitation or other events.

Once the new T_b threshold was determined, the AMSR-E 36.5V GHz data, along with melt onset and spring transition data, were compared with the melt onset results of the SSM/I 37V GHz data for all six of the Wheaton River basin 25 x 25 km^2 pixels (Figs. 6a and 6b, Table 4). This allowed for a new DAV threshold to be created for the AMSR-E data (Table 2), since the daily fluctuations appear to have increased with the AMSR-E sensor, and also helped to determine if the new thresholds are effective at detecting snowmelt as related to previous snowmelt onset detection studies using SSM/I T_b data.

After determining that similar snow melt onset results could be obtained from AMSR-E and SSM/I T_b data gridded at the same 25 x 25 km^2 resolution, the effectiveness of the AMSR-E sensor's improved spatial resolution was investigated. The AMSR-E swath data were gridded to the EASE-Grid with a resolution of 12.5 x 12.5 km^2, which is more representative of the 12 km mean spatial resolution of the 36.5V GHz channel (Ashcroft and Wentz, 2004). This gridded resolution allowed for the creation of four finer resolution pixels of information for each 25 x 25 km^2 pixel (Fig. 1b). Elevation data were used to identify the fine-resolution pixels within any

coarse-resolution pixel with the highest and lowest mean elevations (Table 5). The AMSR-E 36.5V GHz T_b for these pixels, as well as the snowmelt onset timing, were then compared with the coarser 25 x 25 km^2 data to examine the effects of the AMSR-E sensor's increased spatial resolution on improving the ability to detect snowmelt in heterogeneous terrain (Figs. 7a and 7b, Table 5).

Table 3. Spring 2005 Wheaton River basin snow wetness measurements and AMSR-E 25 km^2 T_b

Pit ID	Date & Time (PST)	Latitude (°)	Longitude (°)	Depth (cm)	# of Samples	Average Wetness (%)	AMSR-E 25 km^2 Pixel	AMSR-E 25 km^2 T_b (K)
1	3/24/05 12.48	60.13	-134.88	0	0	n/a	B02	245.2
				0.5 - 2	2	3.12		
2	3/24/05 13.68	60.13	-134.88	0	1	0.47	B02	244.0
				0.5 - 2	3	1.56		
3	3/24/05 14.16	60.23	-135.17	0	0	n/a	B02	244.0
				0.5 - 2	4	1.45		
4	3/27/05 13.20	60.21	-135.27	0	6	0.97	B03	232.9
				0.5 - 2	7	1.40		
5	3/28/05 14.16	60.35	-135.03	0	3	1.55	C03	238.0
				0.5 - 2	6	1.96		
6	3/28/05 14.64	60.35	-135.03	0	3	1.24	C03	238.0
				0.5 - 2	4	1.42		
7	4/1/05 12.96	60.35	-135.07	0	6	1.57	B03	230.8
				0.5 - 2	6	1.75		
8	4/1/05 14.88	60.36	-135.04	0	5	1.30	C03	242.1
				0.5 - 2	5	1.49		
9	4/4/05 11.76	60.29	-135.00	0	8	2.72	B02	251.1
				0.5 - 2	8	2.60		
10	4/4/05 13.44	60.30	-134.99	0	5	2.71	B02	252.0
				0.5 - 2	5	2.25		
11	4/4/05 15.36	60.29	-134.98	0	6	3.23	B02	252.0
				0.5 - 2	6	2.58		
12	4/6/05 13.44	60.23	-135.17	0	5	4.40	B02	254.9
				0.5 - 2	5	2.84		
13	4/6/05 15.12	60.34	-135.00	0	5	3.79	C03	259.4
				0.5 - 2	5	2.97		
14	4/11/05 13.68	60.13	-134.88	0	5	3.30	B02	248.6
				0.5 - 2	5	2.58		

RESULTS

The two main techniques used to determine a new snowmelt onset T_b threshold for the AMSR-E 36.5V GHz channel both found the threshold between non-melting and melting snow to be 252 K. The first method, in which the T_b for the six Wheaton basin pixels were compared with air temperature data for 2004 and 2005 (refer to Fig. 3), illustrates that a T_b threshold of around 252 K is an effective boundary between (1,2) non-melting and (3) melting snow near 0°C. In these non-linear plots, it can be noted that two distinct relationships occur on either side of the 0°C mark. Below 0°C, the T_b are below 252 K and increase very slightly with an increase in temperature. As the temperature approaches and exceeds 0°C, the T_b rapidly increases above 252 K (Fig. 3). This rapid change in the slope of T_b when the air temperature is near 0°C at T_b = 252 K is due to the high sensitivity of microwaves to liquid water within the melting snowpack. The transition from frozen to melting snow is especially clear for pixel B02, which contains the site of the near-surface air temperature observations, as the change in slope between these two conditions at 0°C occurs at the T_b threshold of 252 K (Fig. 3).

It is also worth noting that two distinct distributions of T_b occur when compared to air temperatures below 0°C (Fig. 3). The upper T_b response (Fig. 3, #1) is from periods in November from both 2004 and 2005, while the lower response (Fig. 3, #2) is from periods in December of the same years. The cause of the upper response may be related to ice accumulation on trees during the earlier winter months, a condition that was observed in the 2006 winter season. During the winter, especially during unusually warm years, open lakes that have not yet frozen can create

an icy fog that creeps up valleys and allows for ice to accumulate on vegetation. These distinct distributions may also be an effect of grain size growth during the early winter months, influencing the scattering properties of the snowpack. At the 36.5 GHz frequency, emissivity decreases proportional to an increase in grain size (Mätzler, 1994), and so as the grains within the snowpack grow early in the winter, their T_b decreases from the upper distribution to the lower distribution (Fig. 3). As these events both occur within the same time frame, further investigation is required to identify the source of these differing relationships.

The second technique, examining a histogram of AMSR-E 36.5V GHz T_b distribution from the Wheaton basin for all 2004 and 2005 data, also produced a T_b threshold of 252 K (Fig. 4). The frequency histogram, with a bin size of 2 K, displays a bimodal distribution from which it is interpreted that brightness temperatures less than 252 K relate to frozen, non-melting snow and brightness temperatures greater than 252 K relate to wet, melting snow as well as no snow during the summer months. The sets of individual pixels, representing the upper (pixels A02 and A03), middle (pixels B02 and B03), and lower (pixels C02 and C03) portions of the Wheaton River basin, do not have as clear a bimodal distribution but do have comparable minimum values around 252 K (Fig. 4). This, along with the plots of T_b against air temperature, suggests that the T_b threshold is effective in differentiating between dry and wet snow at the drainage basin and sub-drainage basin scales in this heterogeneous terrain.

The DAV calculation, which involves taking the difference between night and day observations, shows the daily contrast in brightness temperatures at this time of year. The timing of the AMSR-E overpasses for this region are around 03:30 and 13:30 local time (PST), which are likely near the times of minimum and maximum daily melt, and so the difference in the T_b from these times provides a good indicator of melting and refreezing snow. The DAV threshold increased due to the apparent increased sensitivity of the AMSR-E sensor to daily T_b fluctuations (Fig. 6a). A new DAV threshold of ±18 K, which was determined by comparing the AMSR-E DAV with SSM/I DAV for the Wheaton River pixels in 2005 (Fig. 6b), represents times when strong melt-refreeze cycles are occurring during the spring snowmelt transition.

The change in T_b and DAV thresholds from SSM/I to AMSR-E (Table 2) is most likely the result of differences in the times of data acquisition for the two sensors. Daily AMSR-E overpasses for the area occur around 03:30 and 13:30 PST, whereas SSM/I overpasses occur around 08:30 and 18:30 PST. The AMSR-E sensor makes observations during the early morning, when temperatures and corresponding T_b would be near their daily minimum, and again in the early afternoon, when much of the mountainous terrain would be near the daily maximum air and brightness temperatures. This creates larger DAV in relation to the DAV from SSM/I, since the timing of SSM/I overpasses is further from these daily minimum and maximum, and therefore requires a larger DAV threshold. In addition, the DAV threshold must increase so as to not indicate that melting is occurring when large DAV are observed during the summer, when much of the land is snow-free (Fig. 6b).

Field-observed snow liquid-water content measurements from the Wheaton River basin during the spring of 2005 support the T_b threshold of 252 K and also show that the assumed response in T_b to melting snow can be directly attributed to snowmelt instead of other effects, such as liquid precipitation events. Surface (0 cm) and near surface (0.5-2 cm) wetness measurements relate very well to AMSR-E 36.5V GHz T_b observations obtained at coincident times (Figs. 5a and 5b, Table 3). At wetness values below 2%, the T_b are clustered between 230 K and 245 K, but as the liquid-water content of the snowpack increases above 2% by volume, the T_b appear to increase near and above the threshold of 252 K (Fig. 5a). For the period prior to and including the beginning of the spring transition, the changes in the snowpack wetness through time closely follow that of the AMSR-E T_b, and at wetness values above 2%, the T_b are at or above the 252 K threshold (Fig. 5b). This relationship verifies that the T_b response is due to the presence of liquid water within melting snow.

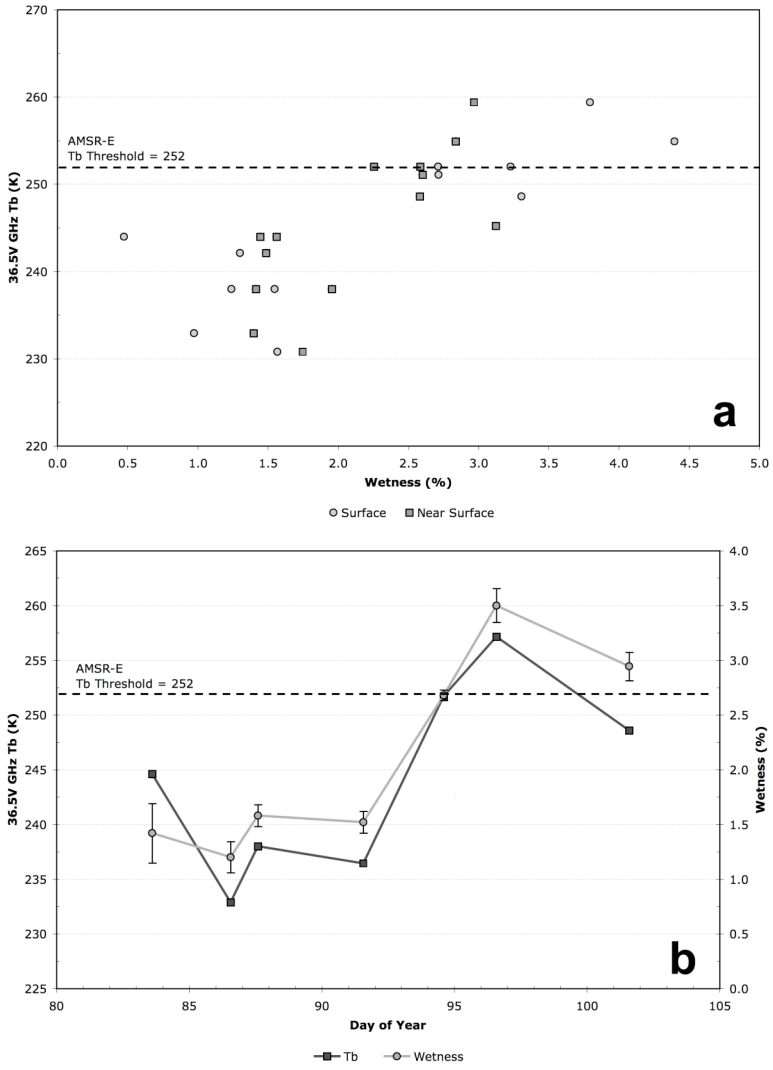

Figure 5. (a) Scatterplot of snowpack wetness compared to AMSR-E 36.5V GHz T_b within the Wheaton River basin. Below 2% wetness, T_b are clustered between 230 K and 245 K, but an increase in liquid-water content beyond 2% creates an abrupt rise in T_b around the threshold of 252 K. (b) The snowpack wetness (gray) relates well to the AMSR-E T_b (black) during the period prior to the spring transition.

With these new AMSR-E snowmelt onset thresholds (T_b > 252 K and DAV > ±18 K), the AMSR-E spring transition in 2004 and 2005 was characterized for the six Wheaton River 25 x 25 km^2 pixels and compared with SSM/I data for the same pixels and years (Figs. 6a and 6b, Table 4). The snowmelt onset algorithm developed by Ramage *et al.* (2006) was used for the SSM/I data, using thresholds of T_b > 246 K and DAV > ±10 K (Table 2). For pixel B02, the onset of snowmelt compares very well between AMSR-E and SSM/I, as does the end of the spring transition and the total duration (Figs. 6a and 6b). It should be noted that although the AMSR-E thresholds were met for this pixel around day 95, they were not met for a consistent length of time, and so the spring transition is interpreted as beginning about 10 days later (Figs. 6a and 6b). The DAV of the AMSR-E observations are higher than the corresponding SSM/I observations throughout the spring transition as well as for much of the summer. Preliminary investigations of AMSR-E derived snowmelt in the larger Pelly River basin, approximately 250 km northwest of the Wheaton River basin, indicate the AMSR-E T_b and DAV thresholds are effective for detecting snowmelt on a regional scale.

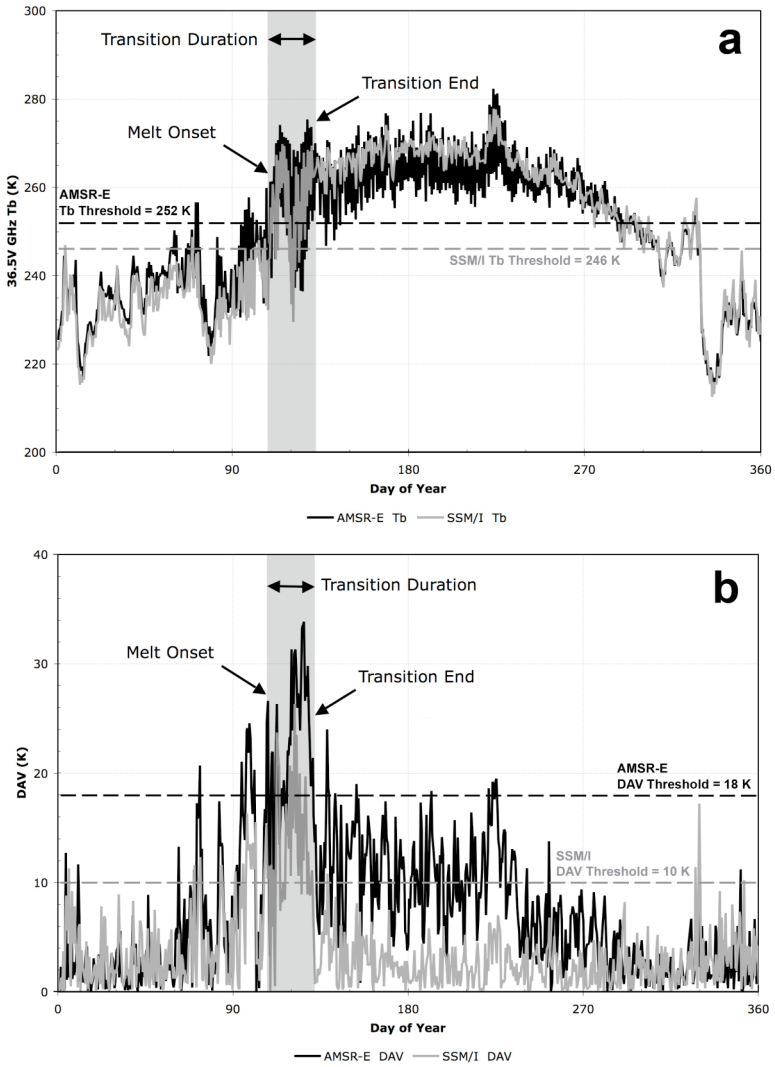

Figure 6. (a) Comparison of pixel B02 AMSR-E and SSM/I T_b for 2005. The AMSR-E T_b (black) match closely with the SSM/I T_b (gray), although they appear to show greater variability during the spring transition and summer months. The melt onset date and duration for the two records are also similar. (b) Comparison of pixel B02 AMSR-E and SSM/I DAV for 2005. The AMSR-E DAV (black) is consistently higher than the SSM/I DAV (gray) throughout the spring and summer. The AMSR-E DAV threshold of ±18 K appears to match with the SSM/I DAV threshold of ±10 K and the timing of SSM/I melt onset.

Table 4. AMSR-E and SSM/I melt dates (day of year) for the Wheaton River Basin

	2004		2005	
Pixel ID	AMSR-E Melt Onset (Day)	SSM/I Melt Onset (Day)	AMSR-E Melt Onset (Day)	SSM/I Melt Onset (Day)
A02	100	100	112	110
A03	116	115	111	110
B02	100	99	110	109
B03	116	116	110	112
C02	95	96	94	94
C03	96	97	106	105

For both 2004 and 2005, the AMSR-E and SSM/I melt onset dates for the six Wheaton River 25 x 25 km^2 pixels match up very well, with the dates differing by less than two days (Table 4). Pixel B03 in 2004 was found to have the same melt onset date for both sensors, as was pixel C02 in 2005. These well correlated melt onset dates indicate that the new AMSR-E data and thresholds are effective in detecting snowmelt in the Wheaton River basin at the same resolution as SSM/I. In addition, this relationship may eventually allow for the observations from both sensors to be combined to create an even more robust satellite record of observation.

Since the AMSR-E sensor provides enhanced resolutions over the SSM/I sensor, especially in the 36.5 GHz channel, the timing of snowmelt within the Wheaton River basin was also determined using T_b data gridded to the EASE-Grid 12.5 x 12.5 km^2 resolution (Fig. 1b). Pixel B02 (25 x 25 km^2 resolution) and the four finer-resolution pixels within it were examined in an attempt to tease out the effects of the heterogeneous terrain on snowmelt onset (Table 5). Differences between the plots of AMSR-E T_b in the first half of 2005 for pixels B02C and B02B, which represent the highest and lowest mean elevations within pixel B02 respectively, indicate that the spatial resolution of the AMSR-E sensor improves upon the SSM/I sensor's ability to detect snowmelt in mixed terrain, especially in areas with a range of elevations (Figs. 7a and 7b, Table 5).

Table 5. EASE-Grid 12.5 x 12.5 km^2 pixel characteristics and melt onset dates for 2005

Pixel ID	Melt Onset (Day)	Transition End (Day)	Transition Duration (Days)	Mean Elevation (m)	Minimum Elevation (m)	Maximum Elevation (m)	Relief (m)
B02*	110	131	21	1177	672	2193	1521
B02A	110	131	21	976	672	1875	1203
B02B	96	131	35	940	696	2160	1464
B02C	110	154	44	1493	711	2193	1482
B02D	109	132	23	1170	719	1842	1123

*This EASE-Grid 25 x 25 km^2 pixel is compared with the four finer-resolution 12.5 x 12.5 km^2 pixels contained within it

In relation to the 2005 melt onset timing and spring transition duration for pixel B02, the timing of these events for the finer-resolution pixels is similar (Table 5). Two notable exceptions are pixel B02B, the lowest in mean elevation, and pixel B02C, the highest in mean elevation. Melt onset occurs much earlier in B02B than in the other pixels, most likely as a result of warmer temperatures within its lower elevations. For B02C, the spring transition period lasts more than 20 days longer than the other pixels, and this is due to colder temperatures in the higher elevations keeping the nighttime snowpack frozen and DAV high well into the spring. Examining the time during which snowmelt onset has begun for B02B (Fig. 7b), it can be noted that the T_b for B02B are consistently above the threshold from day 94 to 100, whereas the T_b for B02C never reach the threshold during this period. Furthermore, T_b for pixel B02 indicate melting during the day from days 96 to 100, and while this concurs with B02B, it disagrees with B02C, and so the higher resolution AMSR-E data is more effective at differentiating melting and non-melting areas in this heterogeneous terrain than lower resolution AMSR-E and SSM/I data.

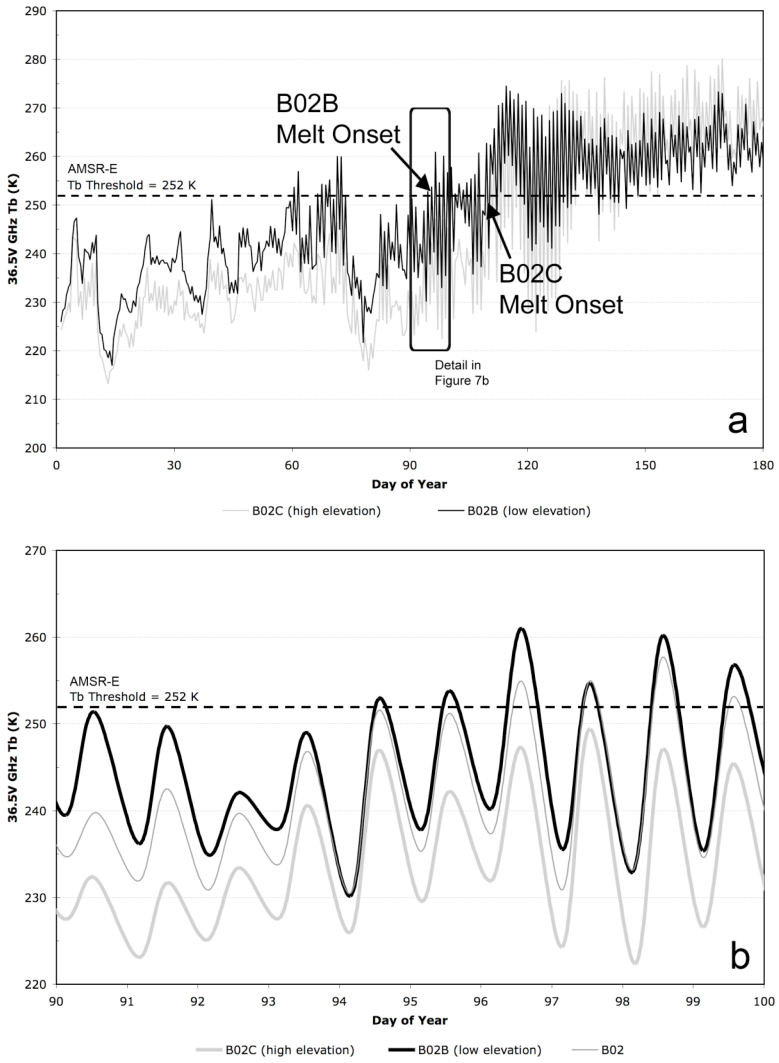

Figure 7. (a) Comparison of higher resolution AMSR-E T_b from 2005 for pixels B02B and B02C. The lower elevation B02B (black) has higher overall T_b than B02C (gray) that relate to warmer temperatures. This results in an earlier melt onset for B02B in relation to B02C and the other pixels (Table 5). (b) A detailed look at days 90 to 100 reveals that the T_b threshold is met consistently in the lower elevations of B02B (black) but not in the higher elevations of B02C (thick gray). Pixel B02 (thin gray) is more closely related to B02B, but the T_b threshold is not met as early as in B02B.

CONCLUSIONS

AMSR-E passive microwave data can be used to investigate snowmelt at the basin and regional scales. In addition, the finer resolution of AMSR-E over that of SSM/I allows for the snowpack characteristics of areas with heterogeneous terrain to be more accurately examined. For the Wheaton River dataset, AMSR-E is more sensitive to daily brightness temperature fluctuations than SSM/I at the same spatial scale. Relating the two datasets at the same scale provides the foundation for a longer-term study of snowmelt dynamics combining the historical record of both sensors. Plots of AMSR-E T_b and near-surface air temperatures, as well as a bimodal distribution of T_b and comparisons with snow liquid-water content, suggest a T_b threshold of 252 K can be used to make the distinction between melting and non-melting snow in combination with a DAV

threshold of ±18 K that reflects the spring transition when large melt-refreeze cycles are occurring. The larger oscillations in daily T_b are most likely due to the timing of data acquisition being closer to the actual maximum and minimum daily T_b. The snowmelt onset algorithm will also be applicable in most arctic and subarctic landscapes.

Snowmelt onset dates from AMSR-E, as determined using the new T_b and DAV thresholds, compare very well with SSM/I for the Wheaton River basin, differing by a maximum of two days. The enhanced spatial resolution of the AMSR-E data provides an improvement over SSM/I in detecting snowmelt onset in areas of mixed terrain. Using this AMSR-E melt onset algorithm, the snowpack dynamics of the Wheaton River basin, as well as other areas of the upper Yukon River basin, can be further investigated spatially and temporally for the record of AMSR-E observations. The improvements by the AMSR-E sensor upon SSM/I allow for a more effective spatial and temporal examination of snowmelt dynamics in the heterogeneous terrain of the upper Yukon River basin. It will be a significant improvement to our ability to understand the melt processes and timing in an important, remote, high latitude drainage basin.

ACKNOWLEDGEMENTS

We would like to extend our thanks to Mary Jo Brodzik, Amanda Leon, and the National Snow and Ice Data Center for EASE-grid satellite data and continued assistance. Thanks to Environment Canada for ongoing support with field logistics and additional data. We thank Sarah Kopczynski and Shannon Haight for their assistance collecting field data. We are also thankful for helpful comments provided by Andrew Klein and two anonymous reviewers. Additional thanks to Michael Chupa. Funding was provided by Lehigh University and the National Aeronautics and Space Administration's Terrestrial Hydrology Program (grant # NNG04GR31G).

REFERENCES

Aagaard K, Carmack EC. 1989. The role of sea ice and other freshwater in the Arctic circulation. *Journal of Geophysical Research* **94**: 14485-14498.

Abdalati W, Steffen K 1997. Snowmelt on the Greenland Ice Sheet as derived from passive microwave satellite data. *Journal of Climate* **10**: 165-175.

Ashcroft P, Wentz F. 2004 updated daily. AMSR-E/Aqua L2A Global swath spatially-resampled brightness temperatures (Tb) V001. January 2004 to December 2005. Boulder, CO, USA: National Snow and Ice Data Center. Digital media.

Brabets TP, Wang B, Meade RH. 2000. *Environmental and hydrologic overview of the Yukon River basin, Alaska and Canada*. USGS Water Resources Investigations Report 99-4204, Anchorage.

Denoth A. 1989. Snow dielectric measurements. *Advances in Space Research* **9**: 233-243.

Derksen C, Walker AE, Goodison BE, Strapp JW. 2005. Integrating *In Situ* and multiscale passive microwave data for estimation of subgrid scale snow water equivalent distribution and variability. *IEEE Transactions on Geoscience and Remote Sensing* **43**: 960-972.

Environment Yukon. 2000. *90 Meter Yukon Digital Elevation Model*. http://www.environmentyukon.gov.yk.ca/geomatics/data/90m_dem.html [13 March 2005].

Foster JL, Chaojiao S, Walker JP, Kelly RE, Chang A, Dong J, Powell H. 2005. Quantifying the uncertainty in passive microwave snow water equivalent observations. *Remote Sensing of Environment* **94**: 187-203.

Goita K, Walker AE, Goodison BE. 2003. Algorithm development for the estimation of snow water equivalent in the boreal forest using passive microwave data. *International Journal of Remote Sensing* **24**: 1097-1102.

Josberger EG, Mognard NM. 2002. A passive microwave snow depth algorithm with a proxy for snow metamorphism. *Hydrological Processes* **16**: 1557-1568.

Kelly RE, Chang AT, Tsang L, Foster JL. 2003. A prototype AMSR-E global snow area and snow depth algorithm. *IEEE Transactions on Geoscience and Remote Sensing* **41**: 230-242.
Kim EJ, England AW. 2003. A yearlong comparison of plot-scale and satellite footprint-scale 19 and 37 GHz brightness of the Alaskan North Slope. *Journal of Geophysical Research* **108**: ACL 7.
Mätzler C. 1994. Passive microwave signatures of landscapes in winter. *Meteorology and Atmospheric Physics* **54**: 241-260.
Ramage JM, Isacks BL. 2002. Determination of melt-onset and refreeze timing on southeast Alaskan icefields using SSM/I diurnal amplitude variations. *Annals of Glaciology* **34**: 391-398.
Ramage JM, Isacks BL. 2003. Interannual variations of snowmelt and refreeze timing on southeast-Alaskan icefields, U.S.A. *Journal of Glaciology* **49**: 102-116.
Ramage JM, McKenney RA, Thorson B, Maltais P, Kopczynski SE. 2006. Relationship between passive microwave-derived snowmelt and surface-measured discharge, Wheaton River, Yukon Territory, Canada. *Hydrological Processes* **20**: 689-704.
Ulaby FT, Moore RK, Fung AK. 1986. *Microwave Remote Sensing: Active and Passive, Vol. III: From Theory to Applications*. Artech House: Dedham.
Vorosmarty CJ, Hinzman LD, Peterson BJ, Bromwich DH, Hamilton LC, Morison J, Romanovsky VE, Sturm M, Webb RS. 2001. *The Hydrologic Cycle and its Role in Arctic and Global Environmental Change: A Rationale and Strategy for Synthesis Study*. Arctic Research Consortium of the U.S.: Fairbanks, Alaska; 84.
Walker AE, Goodison BE. 1993. Discrimination of a wet snowcover using passive microwave satellite data. *Annals of Glaciology* **17**: 307-311.
Wang L, Sharp M, Brown R, Derksen C, Rivard B. 2005. Evaluation of spring snow covered area depletion in the Canadian Arctic from NOAA snow charts. *Remote Sensing of Environment* **95**: 453-463.